

Direct numerical simulation of the combustion of a suspended droplet in normal gravity

A.E. Saufi^a, A. Frassoldati^a, T. Faravelli^a, A. Cuoci^a

^a*Department of Chemistry, Materials, and Chemical Engineering G. Natta, P.zza Leonardo da Vinci 32, Milano, Italy*

Abstract

DropletSMOKE++ is a multiphase CFD framework based on OpenFOAM[®], originally developed and validated for suspended droplets evaporation in a gravity field and convective conditions. In this work the solver is further extended to account for gas-phase combustion introducing: (i) an operator-splitting methodology to efficiently solve the gas-phase chemistry with large kinetic mechanisms, (ii) a model for the flame radiative heat transfer and (iii) a double vaporization model to account for possible boiling. This allows to simulate the combustion of suspended fuel droplets in normal gravity with a detailed description of the gas-phase chemistry, representing the novelty and the main objective of this work. The numerical model is applied to simulate the vaporization, ignition and combustion of a methanol droplet suspended on a quartz fiber at different oxygen concentrations. The numerical results are compared with recent experimental data, showing a satisfactory agreement in terms of diameter decay, radial temperature profiles and sensitivity to the oxygen concentration in the gas-phase. In particular, the burning rate is found to be significantly affected by thermal conduction from the fiber, due to its relatively large size and the high temperatures involved in the combustion process. On the other hand the fiber perturbs the flame itself, providing a partial quenching close to its surface. The droplet combustion behavior has been compared to the one predicted in microgravity conditions, evidencing a lower standoff ratio, a higher flame temperature and an intense internal circulation. The gas-phase chemistry has been analyzed in terms of distribution of the main species in the gas phase, showing a local accumulation of (i) intermediate oxidation products at the fiber (due to the quenching) and (ii) water at the surface, which partially condenses on the droplet surface affecting the vaporization rate.

arXiv:2005.02866v1 [cs.CE] 5 May 2020

Keywords:

droplet combustion, gravity, VOF, support fiber, methanol

1. Introduction

Spray and droplet combustion technologies are adopted in a large number of practical applications: power generation, propulsion, fuel injectors for diesel engines and aerospace applications. The combustion of a spray of droplets evolves through three main steps: (i) the atomization of the liquid, (ii) the vaporization of the fuel droplets and (iii) the ignition of the gas-phase and the subsequent combustion. Even though the numerical simulation of these systems is rapidly advancing, major difficulties remain due to the intrinsic complexity of the problem: droplets breakup, coalescence, surface tension instabilities, interactions with a turbulent gas flow are very complex phenomena, not yet fully understood [1, 2]. Evaporation and gas-phase combustion create large spatial temperature and concentration gradients, which further complicate the problem. Moreover, these phenomena are strongly coupled and they occur at very different temporal and spatial scales (several orders of magnitude), making their numerical modeling extremely expensive. Hence, the need of simplified but still physically representative configurations.

In particular, the study of the evaporation and combustion of a single isolated droplet represented an essential step towards the better understanding of more complex systems, both experimentally and numerically. In the last decades researchers mainly focused on a simple, idealized condition in which a spherical droplet was investigated in microgravity [3, 4], because of the absence of buoyancy effects and droplet deformation. This was also attractive for the relatively simple mathematical modeling, exploiting the spherical symmetry of the system and leaving room for a more detailed chemistry description [5, 6]. This paved the way for the study of crucial aspects related to droplets combustion such as cool flames, multiple ignitions and extinction phenomena [7, 8]. Even if the microgravity condition still represents a valuable method for droplets analysis, there is a strong interest in considering more realistic situations in which convection and gravity play a significant role (like in sprays). The most common case is represented by the vaporization, ignition and combustion of a single droplet suspended on a fiber in normal gravity

[9, 10, 11, 12, 13]. This system requires additional complexity in the mathematical description with respect to the zero-gravity case. In particular, a CFD multiphase model is required, including: (i) a robust numerical method for the interface localization and advection, (ii) the solution of both a gas and liquid velocity field, (iii) a reliable model for evaluating the evaporation rate in convective conditions and (iv) a multi-region approach to model the flame-fiber thermal interaction [14]. In this context, while noteworthy papers can be found for pure evaporation in normal gravity [15, 16, 17], very few numerical works on combustion are available and mainly limited to non-shrinking, motionless droplets [18] or adopting one-step/global schemes for chemistry [19]. Recently, a skeletal mechanism (~ 20 reactions) was used by Ghata et al. [20] within a multiphase approach, limiting however the application to microgravity conditions. To the authors knowledge, there is a lack of comprehensive models for droplets combustion in convective conditions, coupled with a detailed description of the gas-phase chemistry. The `DropletSMOKE++` solver [21, 22] is a multiphase CFD code specifically conceived to model the evaporation of pure and multicomponent suspended droplets (including i, ii, iii, iv). The main objective of this work is the extension of `DropletSMOKE++` to describe the combustion of suspended fuel droplets with a high level of detail, including:

- An operator-splitting approach to implement a detailed kinetic mechanism within a multi-phase fluid dynamics;
- An optically-thin sub-model for the radiative heat transfer;
- A double vaporization model to account both for thermodynamically driven (evaporation) and thermally driven (boiling) cases.

The recent experimental work of Yadav et al. [23] on methanol droplets has been adopted as a benchmark case for the model validation: a methanol droplet is suspended with on a quartz vertical fiber (at ambient temperature and pressure) and ignited with a spark, tracking the combustion phenomena and the droplet characteristics over time. The numerical modeling of this configuration is the objective of this work and the paper organization reflects this purpose, including: a description of the main mathematical model (Section 3), the numerical methodology (Section 4)

and the main numerical results compared with the experiments (Section 5). In addition, numerical analyses for the thermal effect of the fiber, the flame properties, the main species distribution and water condensation are provided, before moving to conclusions.

2. Experimental setup

The experiments are carried out in a closed combustion chamber (70x70x100 mm³) in which a methanol droplet ($D_0 = 1.8$ mm) is suspended with a syringe on a quartz vertical fiber ($D_f = 0.6$ mm) at 300 K and atmospheric pressure. Two steel electrodes initiate the combustion, which is followed in two ways: a digital camera (60 fps) tracks the droplet surface regression, while a Mach Zehnder interferometer provides the whole temperature field distribution in a non-intrusive manner. More details about the experimental device can be found in the reference work [23].

3. Mathematical model

DropletSMOKE++ is a multiphase CFD code based on the VOF methodology for the interface advection. In addition to the governing equations enforcing the conservation of momentum, energy and species mass, a detailed description of the interface thermodynamics is implemented (based on cubic Equations of State). The evaporation rate \dot{m} is directly calculated from the gas-phase boundary layer and a multiregion approach for the thermal perturbation of the fiber on the droplet is included.

3.1. Interface advection

The VOF methodology [24] is an interface capturing method within an Eulerian formulation, adopting a marker function α to represent the fluid phases. The marker function α represents the liquid volumetric fraction, assuming value 0 in the gas-phase and value 1 in the liquid phase. The following equation for α is solved:

$$\frac{\partial \alpha}{\partial t} + \nabla \cdot (\mathbf{v}\alpha) = \frac{\dot{m}}{\rho} - \frac{\alpha}{\rho} \frac{D\rho}{Dt} \quad (1)$$

where the source terms represent the contribution of the evaporation/condensation rate (depending on the sign of \dot{m}) and the droplet dilation due to the change of density $\frac{D\rho}{Dt}$. The interface

is advected using the `isoAdvector` library [25] developed by Roenby and Jasak, reconstructing the interface with a geometrical approach. The performances are superior to the MULES compressive scheme [26] commonly adopted in `OpenFOAM`[®], in terms of shape preservation, volume conservation, interface sharpness and efficiency.

3.2. Governing equations

The velocity field is shared between the two phases, solving a single Navier-Stokes equation in the whole computational domain:

$$\frac{\partial(\rho\mathbf{v})}{\partial t} + \nabla \cdot (\rho\mathbf{v} \otimes \mathbf{v}) = \nabla \cdot \mu (\nabla\mathbf{v} + \nabla\mathbf{v}^T) - \nabla p_{rgh} - \mathbf{g} \cdot \mathbf{x} \nabla \rho \quad (2)$$

where $p_{rgh} = p - \mathbf{g} \cdot \mathbf{x}$ is the dynamic pressure, which greatly simplifies the definition of boundary conditions. The momentum equation is coupled with the following continuity equation:

$$\frac{1}{\rho} \frac{D\rho}{Dt} + \nabla \cdot \mathbf{v} = \dot{m} \left(\frac{1}{\rho_L} - \frac{1}{\rho_G} \right) \quad (3)$$

in which the term $\dot{m} \left(\frac{1}{\rho_L} - \frac{1}{\rho_G} \right)$ provides the interfacial velocity jump due to the phase-change (i.e. Stefan flow). Additionally, the energy equation is included:

$$\rho C_p \left(\frac{\partial T}{\partial t} + \mathbf{v} \nabla T \right) = \nabla \cdot (k \nabla T) - \nabla \cdot \mathbf{q}_{rad} - \nabla T \sum_i^{N_s} \mathbf{j}_i C_{p,i} - \sum_i^{N_{sL}} \dot{m}_i \Delta h_{ev,i} - \sum_j^{N_R} R_j \Delta H_{R,j} \quad (4)$$

The term $\sum_i^{N_{sL}} \dot{m}_i \Delta h_{ev,i}$ accounts for the interface cooling due to the evaporation of the N_{sL} liquid species, while the term $\sum_j^{N_R} R_j \Delta H_{R,j}$ is the energy source term due to the N_R combustion reactions. \mathbf{q}_{rad} describes the radiative heat transfer contribution. \mathbf{j}_i are the diffusion fluxes based on the species mole fractions gradient ∇y_i [27]:

$$\mathbf{j}_i = -\rho \mathcal{D}_i \frac{M_{w,i}}{M_w} \nabla y_i \quad (5)$$

Finally, the chemical species in the gas phase have to be transported:

$$\frac{\partial \rho \omega_i^G}{\partial t} + \nabla \cdot (\rho \mathbf{v} \omega_i^G) = -\nabla \cdot \mathbf{j}_i + \sum_j^{N_R} R_j \nu_{i,j} \quad (6)$$

where the species source term $\sum_j^{N_R} R_j \nu_{i,j}$ is due to the N_R combustion reactions. $\nu_{i,j}$ represent the stoichiometric coefficient of the i -th species in the j -th reaction.

3.3. Interface thermodynamics

At the interface vapor-liquid equilibrium conditions are assumed. Adopting a cubic Equation of State (EoS), the general equation for a two-phase systems is [28]:

$$p_i^0(T) x_i \phi_i(T, p_i^0) e^{\int_{p_i^0}^p \frac{v_{L,i}}{RT} dp} \gamma_i(T, x_i) = p y_i \hat{\phi}_i(T, p, y_i) \quad (7)$$

where $p_i^0(T)$ is the vapor pressure of species i , ϕ_i is the gas-phase fugacity coefficient for the pure species and $\hat{\phi}_i$ is the gas-phase mixture fugacity coefficient. The exponential term represents the Poynting correction, while x_i and y_i are the liquid and gas mole fractions of species i . γ_i is the activity coefficient for non-ideal mixtures. For fuels burning at atmospheric pressure, the equation can be well approximated with a modified Raoult's law:

$$p_i^0(T) x_i \gamma_i = p y_i \quad (8)$$

The equilibrium gaseous mole fraction y_i is evaluated explicitly:

$$y_i = \frac{p_i^0(T)}{p} x_i \gamma_i \quad (9)$$

as well as the equilibrium gaseous mass fraction ω_i^G :

$$\omega_i^G = \frac{p_i^0(T)}{p} x_i \frac{M_{w,i}}{M_w} \gamma_i \quad (10)$$

and assigned to the whole liquid phase. Equation 6 is then solved to advect the gaseous species.

3.4. Evaporation rate

The vaporization flux of each liquid species \dot{m}_i is directly calculated from the gas-phase diffusive contribution \mathbf{j}_i (based on Equation 5) and the total flux \dot{m} at the boundary layer:

$$\dot{m}_i = \mathbf{j}_i \nabla \alpha + \dot{m} \omega_i \quad (11)$$

where $\nabla \alpha$ applies the evaporation flux only at the interface. For monocomponent fuels $\dot{m}_i = \dot{m}$, so Equation 11 can be re-arranged to give the total evaporation rate \dot{m} :

$$\dot{m} = \frac{\mathbf{j}_i}{1 - \omega_i} \nabla \alpha \quad (12)$$

which is equal to \dot{m}_i for monocomponent fuels. If the dot product $\mathbf{j}_i \nabla \alpha$ is negative we have evaporation ($\dot{m} < 0$), otherwise we have condensation ($\dot{m} > 0$). In the same way, the evaporation rate for multicomponent fuels can be easily derived, obtaining:

$$\dot{m} = \frac{\sum_i^{N_{s,L}} \mathbf{j}_i}{1 - \sum_i^{N_{s,L}} \omega_i} \nabla \alpha \quad (13)$$

The total evaporation flux \dot{m} is used as a source term in Equation 1. The evaporation flux of each species \dot{m}_i (only needed for multicomponent cases) can be calculated with Equation 11 once \dot{m} is known.

3.5. Droplet suspension

In normal gravity evaporation experiments, the surface tension force \mathbf{f}_s suspends the liquid droplet against gravity:

$$\mathbf{f}_s = \sigma \kappa \delta_s \mathbf{n} \quad (14)$$

where κ is the interface curvature and δ_s is a Dirac delta applied on the interface. Modeling surface tension is one of the main challenges in multiphase flows, especially at small scales, for two main reasons:

- The surface tension force is only applied at the interface and this makes its numerical discretization very difficult (i.e. the Dirac delta δ_s). Standard or trivial discretization methods are not able to perfectly balance the pressure gradient and the surface tension force, developing artificial velocity spikes at the interface (called spurious currents), which can eventually grow and break the droplet apart;
- Within a VOF approach the interface curvature κ is not easily accessible, due to the discontinuous nature of the marker α :

$$\kappa = \nabla \cdot \mathbf{n} = \nabla \cdot \left(\frac{\nabla \alpha}{|\nabla \alpha|} \right) \quad (15)$$

which makes the interface normal (\mathbf{n}) calculation very difficult. Numerical errors on κ represents another source of spurious currents, in addition to incorrect interface discretizations.

This issue is very well known in literature [29, 30]: available solutions either rely on simple filtering of the α function [31, 32] or more rigorous methods both for the surface tension discretization (e.g. Ghost Fluid Method [33, 34]) and curvature computation (e.g. height functions [35, 30] or least-squares methods [36, 37]). While filtering techniques are proved to be non-consistent [38] and hardly generalizable, rigorous techniques require a great effort to be correctly implemented. In particular, the `OpenFOAM`[®] framework lacks in reliable models for surface tension driven flows and no valid and general solution has been proposed so far. Moreover, the aforementioned methods are not proved to efficiently work in evaporative conditions: the presence of evaporation further worsens the problem, since the Stefan flow tends to destabilize the interface thickness. The research in this sense is still at the beginning and only few results are available [39, 17].

In order to overcome this problem, a centripetal force \mathbf{f}_m directed towards the droplet center is introduced, in order to keep the droplet attached to the fiber and suspended in the presence of a gravity field. In this way the surface tension force is not needed anymore and it can be suppressed, eliminating parasitic currents directly from their source. The Navier-Stokes equation becomes:

$$\frac{\partial(\rho \mathbf{v})}{\partial t} + \nabla \cdot (\rho \mathbf{v} \otimes \mathbf{v}) = \nabla \cdot \mu (\nabla \mathbf{v} + \nabla \mathbf{v}^T) - \nabla p_{rgh} - \mathbf{g} \cdot \mathbf{x} \nabla \rho + \mathbf{f}_m \quad (16)$$

This methodology allows to model the droplet evaporation process whatever the droplet size, without worrying about the detrimental effect of spurious currents. More details about the implementation can be found in the `DropletSMOKE++` reference work [21].

3.6. Multiregion approach for conjugate heat transfer

The fuel droplet is suspended on a vertical fiber and evaporated under a normal gravity field. Numerous experimental and numerical analyses [40, 41, 42] showed that the tethering system can significantly affect the vaporization process from a thermal point of view. The solid is heated by the gaseous environment and conducts heat towards the droplet, providing a preferential path for the heat flux on the liquid. This phenomenon becomes extremely important in combustion processes (due to the high gas temperature) and when adopting large fiber diameters (due to the larger surface available for the heat transfer). The `DropletSMOKE++` code includes a multiregion approach to account for the fiber thermal perturbation, firstly presented in [22]. The heat transfer is modeled considering the real geometry of the fiber, with no need of semi-empirical correlations or approximate approaches to account for the tethering system. The fluid and the solid regions are independently meshed, solved and connected with dynamic boundary conditions, providing a full detailed numerical simulation of the three-phase system. The following equation is solved for the solid phase:

$$\rho_s C_{p,s} \frac{\partial T_s}{\partial t} = \nabla \cdot (k_s \nabla T_s) - \nabla \cdot \mathbf{q}_{rad,s} \quad (17)$$

while the fluid temperature field is provided by Equation 4 and $\mathbf{q}_{rad,s}$ is the radiative heat flux from the fiber. The external surface of the solid fiber is the contact boundary between the phases. The boundary conditions describe the conservation of heat fluxes across the boundary as well as the continuity of temperature.

3.7. Gas, liquid and solid properties

The fluid properties are computed with the `OpenSMOKE++` library [43]. In particular, the gas physical properties ($\rho, \mu, C_p, k, \mathcal{D}_i$) are based on the kinetic theory of gases, while liquid

$(\rho, \mu, C_p, k, \mathcal{D}_i, \Delta h_{ev,i}, p_i^0)$ and solid $(\rho_s, C_{p,s}, k_s)$ properties are evaluated based on the correlations available in the Yaws and Prausnitz [44, 45] databases. The activity coefficient γ_i for non-ideal mixtures is calculated based on the UNIFAC approach [46]. Within a VOF approach, the mixture properties to be used in the governing equations are computed as follows (e.g. for density ρ):

$$\rho = \rho_L \alpha + \rho_G (1 - \alpha) \quad (18)$$

3.8. Combustion modeling

The `DropletSMOKE++` model has been extensively validated for evaporation cases against numerous experimental data [21, 22] in a wide range of operating conditions, both in natural and forced convection. In this work, the model is further extended to include the gas-phase combustion and related phenomena. In particular:

- In order to overcome the stiffness of reacting processes, the gas-phase chemistry implementation is based on an operator-splitting approach [47], separating transport and reaction terms. It was adopted and extensively validated in the `laminarSMOKE++` solver [48] for the modeling of laminar flames with very detailed kinetic mechanisms (hundreds of species and thousands of species). The detailed implementation will be reported in the numerical methodology section;
- An optically thin model is used for radiative heat transfer, considering H_2O , CO , CO_2 and CH_4 as main radiating species. This is justified by the small optical depth of the system ($a_p L|_{max} < 0.3$, where a_p is the maximum local average absorptivity and L the maximum length in the domain). Planck absorption coefficients $a_{p,i}$ are calculated for each species and averaged based on the species mole fractions to obtain a_p :

$$a_p = \sum_i^{N_{s_r}} y_i a_{p,i} \quad (19)$$

where N_{s_r} are the number of radiating species. Radiation is included in the temperature equation as the divergence of the radiating flux:

$$\nabla \cdot \mathbf{q}_{rad} = 4a_p\sigma (T^4 - T_{env}^4) \quad (20)$$

where σ is the Stefan-Boltzmann constant and $T_{env} = 300$ K. Radiation from the solid fiber is also considered in Equation 17, with $a_{p,s} = 0.93$ for quartz [44]:

$$\nabla \cdot \mathbf{q}_{rad,s} = 4a_{p,s}\sigma (T_s^4 - T_{env}^4) \quad (21)$$

- When a droplet evaporates in a mildly-hot (few hundreds degrees K) environment, the liquid surface reaches (after a transient period) a steady wet-bulb temperature, below the liquid boiling point T_b , due to the balance of the incoming heat flux and vaporization enthalpy (Equation 4). The internal liquid temperature is generally lower. The evaporation rate \dot{m} in these conditions is governed by the species diffusion flux \mathbf{j}_i from the surface (Equations 12, 13). On the other hand, the presence of a significant thermal perturbation from the fiber (typical case in combustion processes with a few thousands degrees K) can push the internal liquid temperature towards the boiling point T_b . In this case the liquid temperature profile should reach T_b and instantaneously flatten, remaining constant. However, Equation 4 cannot predict this profile discontinuity inside the liquid phase (the cooling term $\sum_i^{N_{SL}} \dot{m}_i \Delta h_{ev,i}$ is zero outside the interface) and the internal droplet temperature would continue to increase above T_b . In fact, the heat flux per unit volume \dot{q} acting on a point in the droplet is entirely used to vaporize the liquid, maintaining the local temperature constant. Therefore, the vaporization rate in the liquid phase should be calculated as:

$$\dot{m} = -\frac{\dot{q}}{\Delta h_{ev}} = -\frac{\rho C_p \frac{\partial T}{\partial t}}{\Delta h_{ev}} \quad (22)$$

where Δh_{ev} is the vaporization enthalpy. Equation 22 is to be applied at every point in the liquid phase in which $T \geq T_b$. If the liquid is a monocomponent fuel, the species vaporization flux \dot{m}_i is obviously equal to \dot{m} . Equation 22 is also valid for multicomponent droplets, with the only difference that the boiling temperature T_b depends on the local composition x_i

	monocomponent	multicomponent
\dot{m}	$\begin{cases} \frac{\mathbf{j}_i}{1-\omega_i} \nabla \alpha & \text{if } T < T_b \\ -\frac{\rho C_p}{\Delta h_{ev}} \frac{\partial T}{\partial t} & \text{if } T \geq T_b \end{cases}$	$\begin{cases} \frac{\sum_i^{N_{s,L}} \mathbf{j}_i}{1-\sum_i^{N_{s,L}} \omega_i} \nabla \alpha & \text{if } T < T_b \\ -\frac{\rho C_p}{\Delta h_{ev}} \frac{\partial T}{\partial t} & \text{if } T \geq T_b \end{cases}$
\dot{m}_i	\dot{m}	$\begin{cases} \mathbf{j}_i \nabla \alpha + \dot{m} \omega_i & \text{if } T < T_b \\ \dot{m} \frac{p_i^0(T)}{p} x_i \frac{M_{w,i}}{M_w} \gamma_i & \text{if } T \geq T_b \end{cases}$

Table 1: Summary of the vaporization rates \dot{m} (total) and \dot{m}_i (for each species) for monocomponent and multicomponent liquids.

through Raoult’s law (Equation 8) and it should be calculated in every point in the liquid phase. In this case the vaporization flux \dot{m}_i can be calculated from the equilibrium gas-phase mass fraction (Equation 10):

$$\dot{m}_i = \dot{m} \omega_i^G = \dot{m} \frac{p_i^0(T)}{p} x_i \frac{M_{w,i}}{M_w} \gamma_i \quad (23)$$

Since predicting bubbles nucleation and growth is extremely difficult (and beyond the purpose of this work), the internal boiling flux contribution ($T \geq T_b$) is redistributed on the droplet interface to evaluate the interface regression (Equation 1). It is important to point out that in principle boiling occurs at temperatures higher than T_b , due to the superheat needed for bubbles nucleation and to overcome the surface tension energy barrier. However, in the presence of heterogeneous nucleation (due to the presence of the fiber, impurities in the fuel etc.) we can safely assume the superheat to be negligible in this case. The vaporization rate calculations are summarized in Table 1 both for monocomponent and multicomponent droplets.

4. Numerical setup

The DropletSMOKE++ solver is based on the OpenFOAM[®] framework, adopting a finite-volume discretization of the governing equations. These are solved in a segregated approach and adopting the PIMPLE algorithm, a combination between SIMPLE (Semi-Implicit Method for Pressure-Linked Equations) and PISO (Pressure Implicit Splitting of Operators), to manage the pressure-

velocity coupling [49]. The time step size Δt is controlled by the CFL condition governed by the Courant number ($Co < 0.5$), while time integration adopts an implicit Euler method. The spatial discretization is based on Gauss linear scheme for the convective terms, while an orthogonal correction is adopted for Laplacian (diffusive) terms.

4.1. The operator-splitting approach

The operator-splitting approach [47] is the numerical methodology adopted in this work to efficiently include the chemical reactions. The highly non-linear dependence on temperature and species concentration and the very stiff nature of the combustion chemistry make the direct numerical resolution of Equations 4 and 6 extremely difficult. The numerical strategy is the segregation of the transport term and the source term of the governing equations within the same time step. For a generic variable ψ having source term \mathbf{S} and transport term (diffusion, convection etc.) \mathbf{T} :

$$\frac{\partial \psi}{\partial t} = \mathbf{T}(\psi) + \mathbf{S}(\psi) \quad (24)$$

this equation is solved in three sub-steps (Strang splitting):

1. Integration of the source term $\mathbf{S}(\psi)$ over a time step $\Delta t/2$. The initial condition $\psi^{(0)}$ is from the previous time step.

$$\frac{\partial \psi}{\partial t} = \mathbf{S}(\psi) \quad (25)$$

2. Integration of the transport term $\mathbf{T}(\psi)$ over a time step Δt . The initial condition $\psi^{(1)}$ is the result of the first integration (Point 1).

$$\frac{\partial \psi}{\partial t} = \mathbf{T}(\psi) \quad (26)$$

3. Second integration of the source term $\mathbf{S}(\psi)$ over a time step $\Delta t/2$. The initial condition $\psi^{(2)}$ is the result of the second integration (Point 2).

$$\frac{\partial \psi}{\partial t} = \mathbf{S}(\psi) \quad (27)$$

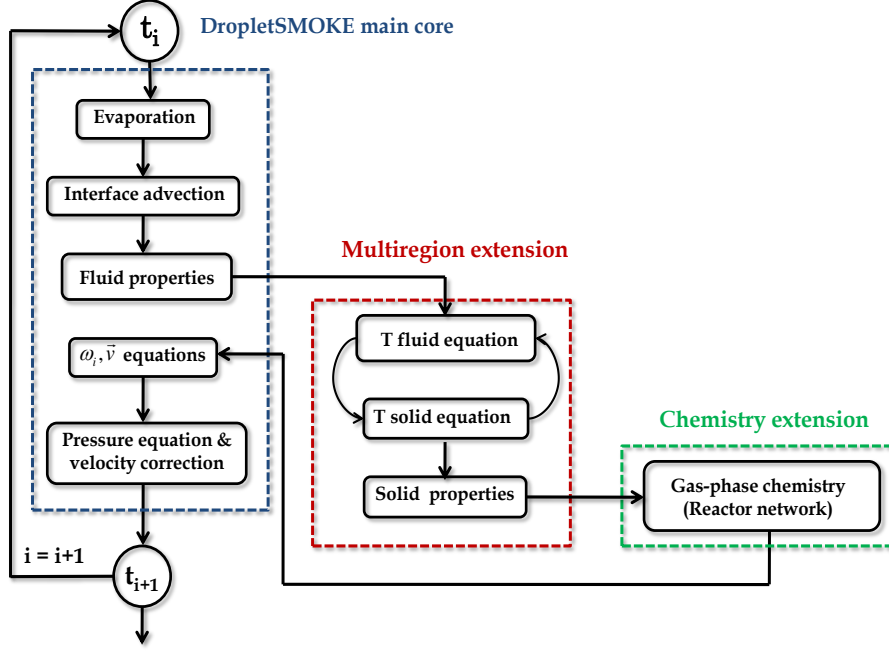


Figure 1: Numerical steps of the `DropletSMOKE++` code, including the multiregion extension for the description of the solid fiber and the reactor network for the combustion chemistry.

The variables ψ are the species mass fractions ω_i and the temperature T . These are solved in a fully coupled approach for points 1 and 3, providing a stiff system of $Ns + 1$ (Ns species and T) non-linear ODE for each computational cell. These ODE systems are totally independent, since the source terms $\mathbf{S}(\psi)$ are local and do not depend on adjacent cells. This is equivalent to the solution of a network of Nc independent batch reactors, where Nc is the number of cells. The numerical resolution is based on the `OpenSMOKE++` library [43], specifically developed to efficiently solve stiff ODE systems and manage detailed kinetic mechanisms. On the other hand, point 2 is solved in a segregated manner for the Ns species and temperature T (as typically done in `OpenFOAM`[®]). Additional details about the implementation can be found in the work of Cuoci et al. [48] (for the `laminarSMOKE++` solver), as well as an extensive validation for laminar flames with detailed kinetic mechanisms. It is important to specify that reactions only occur in the gas-phase: within a VOF approach this requires the resolution of the reactive step only if $\alpha = 0$ in the computational cell of interest. The main numerical steps included in the `DropletSMOKE++` solver are summarized in Figure 1.

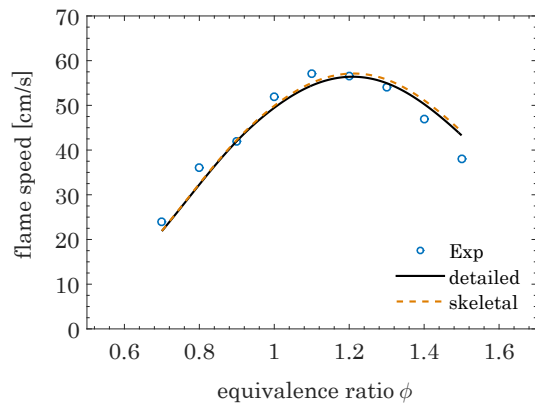


Figure 2: Experimental data of atmospheric laminar flame speeds of methanol at different equivalence ratios and $T_0 = 343$ K from Veloo et al. [50]. Comparison between detailed and skeletal mechanisms.

4.2. Kinetic mechanism

The kinetic mechanism for methanol combustion was obtained from the CRECK kinetic framework, which describes the pyrolysis, partial oxidation and combustion of hydrocarbons up to C_{16} . The C_0 - C_3 mechanism [51] was recently updated following the works of Metcalfe [52] (for H_2/O_2 and C_1/C_2), Burke [53] (for C_3) and implementing the thermodynamics from Burcat database [54]. To limit the computational cost, the resulting mechanism (115 species, 1998 reactions) was finally reduced to a skeletal mechanism (20 species, 129 reactions) using the DoctorSMOKE++ software [55], based on a combination of the Direct Relation Graph with Error Propagation (DRGEP) [56] and a species-targeted sensitivity analysis [57] with a maximum error on the ignition delay time set to 8%. The detailed and the reduced mechanisms are compared in Figure 2, in terms of methanol laminar flame speed. The reduced mechanism is available in the supplementary data.

4.3. Computational mesh

The computational mesh is built with the commercial CFD code Ansys FLUENT[®] v19.2 and then converted in OpenFOAM[®] format. The geometry represents a cylinder (radius L , height H) with a central vertical fiber (radius r) on which the droplet is suspended (Figure 3). Only a slice (5 degrees) of the total geometry is modeled exploiting the axial symmetry. The total number of cells is $\sim 92,000$ for the fluid region and $\sim 10,000$ for the solid region. The resulting droplet resolution is $D/\Delta x \sim 100$, necessary to solve the gas film thickness for the heat and mass transfer rates evaluation. A grid refinement analysis is reported in the appendix, proving mesh independence.

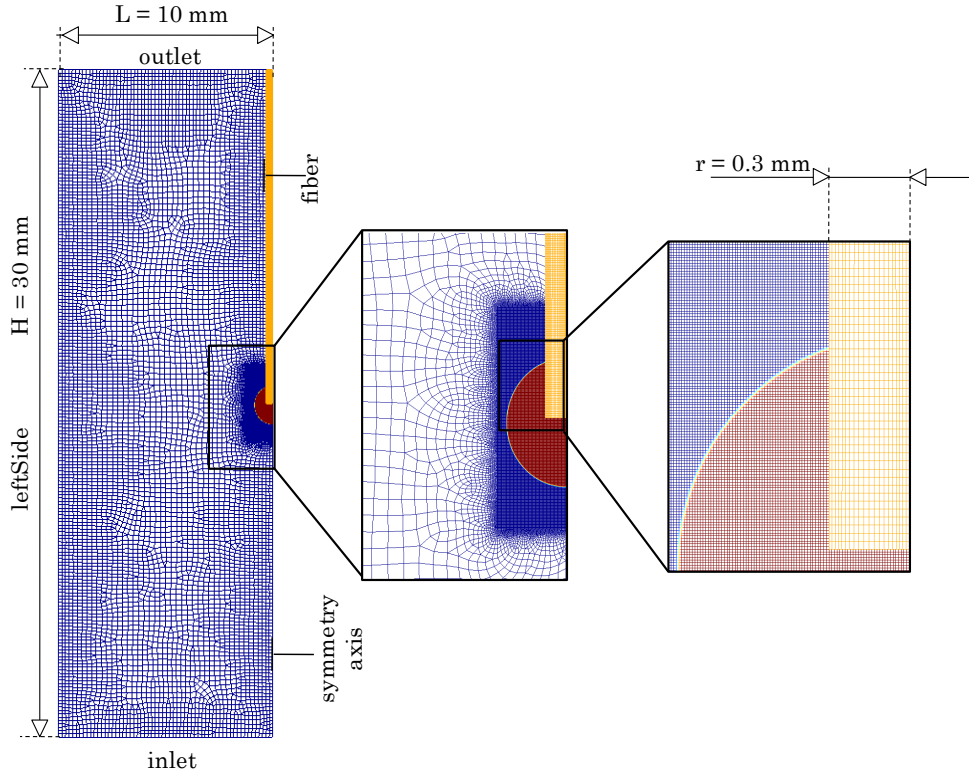


Figure 3: Computational mesh used in this work, with suspended droplet (red region) at three levels of detail. The fluid region (blue) and the solid region (orange) are separately meshed and connected, sharing the **fiber** boundary.

The solid and the fluid regions are meshed independently and then connected with the shared boundary **fiber**. The fluid region is refined around the droplet to provide a sufficiently sharp interface and resolve the boundary layer. The resulting mesh is non-structured, with a non-orthogonality coefficient equal to 57 (safe values are < 70) and a maximum Skewness of 1.56 [49].

4.4. Boundary conditions

There are five boundaries in the computational domain named **leftSide**, **inlet**, **outlet**, **symmetry axis** and **fiber** (Figure 3). The computational geometry is smaller than the real one (in order to reduce the computational cost), therefore the external boundaries **leftSide**, **inlet** and **outlet** are considered open to not perturb the combustion process. Outlet boundary conditions are managed in OpenFOAM[®] as a zero gradient condition, which switches to a fixed value condition if the boundary velocity vector is directed inside the domain (backward flow). The **fiber** boundary condition enforces the thermal fluxes conservation and the continuity of the temperature

Boundary	\mathbf{v}	Temperature	ω_i	p
inlet, outlet, leftSide	open	open	open	$p = p_{ext}$
fiber	$\mathbf{v} = 0$	fluid-solid coupling	$\nabla\omega_i = 0$	$\nabla p = 0$

Table 2: Boundary conditions for velocity \mathbf{v} , temperature T , species mass fraction ω_i and pressure p . The mesh is presented in Figure 3.

Case	D_0 [mm]	y_{O_2} [-]
1	1.8	0.17
2	1.8	0.21
3	1.8	0.25

Table 3: Experimental cases of burning methanol droplets from Yadav et al. [23] examined in this work. y_{O_2} is the initial oxygen mole fraction in the gas-phase. $p = 1$ bar, $T = 300$ K.

profile. The coupled heat transfer is included in the `turbulentTemperatureCoupledBaffleMixed` boundary condition, available in `OpenFOAM`[®] for conjugate heat transfer problems [49]. A summary of the boundary conditions is presented in Table 2.

4.5. Parallelization

The `DropletSMOKE++` code works in parallel mode, adopting the Domain Decomposition Method already included in `OpenFOAM`[®]. Almost $\sim 95\%$ of the CPU time is used for the chemical step (the resolution of the ODE systems). Since this is a local step (no data transfer across the processors is needed), the parallelization efficiency is very high. The simulations presented in this work were run on a multi-processor machine (Intel Xeon X5675, 3.07 GHz). Using 60 processors the average CPU time was $\sim 90 - 100$ h.

5. Combustion of methanol droplets

5.1. Initial conditions

In this work three cases of methanol droplets combustion are considered, varying the oxygen mole fraction in the gas-phase. The cases are summarized in Table 3.

The spark ignition is simulated as a small sphere ($D = 0.1$ mm) having a temperature $T_{spark} = 2500$ K placed at 1 mm from the droplet surface. The spark is applied after a short time of pure evaporation (~ 0.02 s) to facilitate the ignition, for a total duration of 0.05 s. The initial

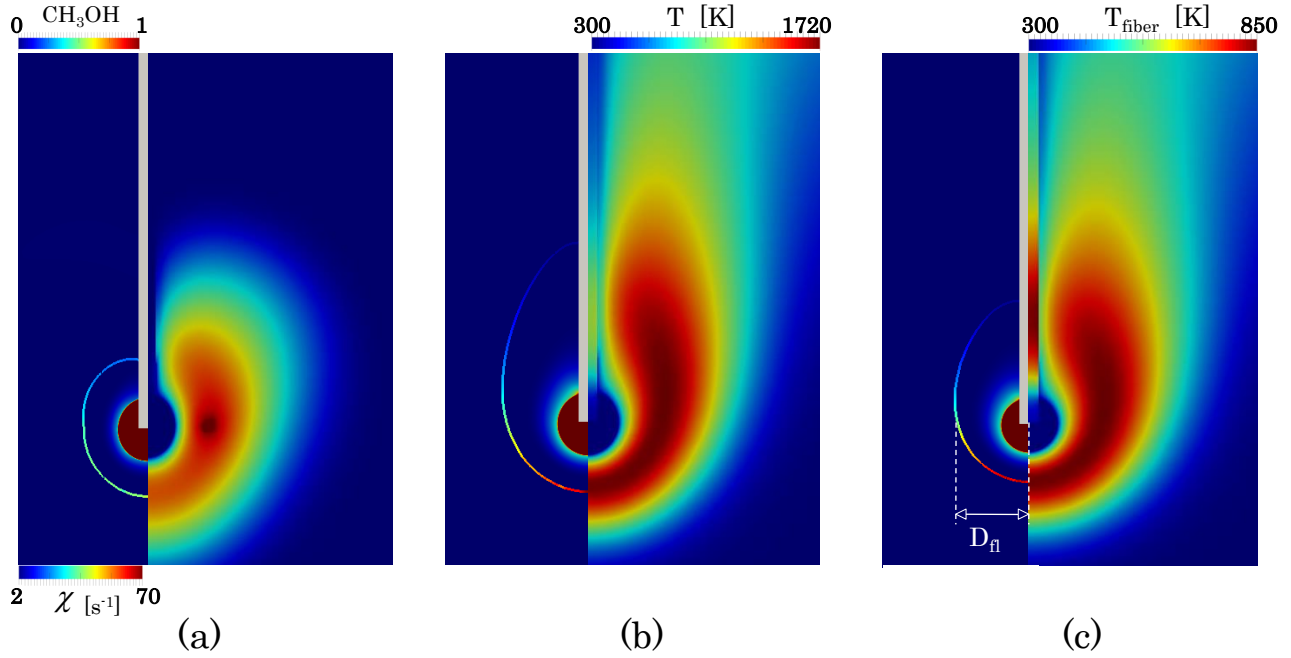


Figure 4: Case 2: 2D maps of methanol mass fraction (left), fluid and solid temperatures (right) at times $t = 0.07$ s (a), $t = 0.5$ s (b) and $t = 1$ s (c). On the left side the stoichiometric passive scalar Z_{st} contour is shown, colored by the scalar dissipation rate $\chi = 2D_{N_2}|\nabla Z|^2$ [58]. The flame diameter D_{fl} definition is evidenced in (c).

conditions for the marker α and for the methanol mass fraction are shown in Figure 3. The fluid and solid initial temperatures are $T = 300$ K and the initial pressure is $p = 1$ bar.

5.2. Ignition and droplet combustion

The ignition and combustion dynamics of Case 2 is qualitatively presented in Figure 4 by means of temperature and methanol mass fraction fields. In Figure 5 the main combustion products (H_2O , CO_2 , CO) and O_2 are presented in terms of mass fractions. The gas-phase ignites at $t \sim 0.07$ s, developing a buoyant diffusion flame. In Figure 4a the ignition spark is still visible close to the droplet surface.

It is useful to analyze the flame structure adopting a passive scalar Z [58]. Following Bilger's approach [59], we define the parameter β :

$$\beta = \frac{2}{M_{w,C}}\omega_C + \frac{1}{2M_{w,H}}\omega_H - \frac{1}{M_{w,O}}\omega_O \quad (28)$$

where the mass fraction of the k -th element (C, H, O) are calculated as:

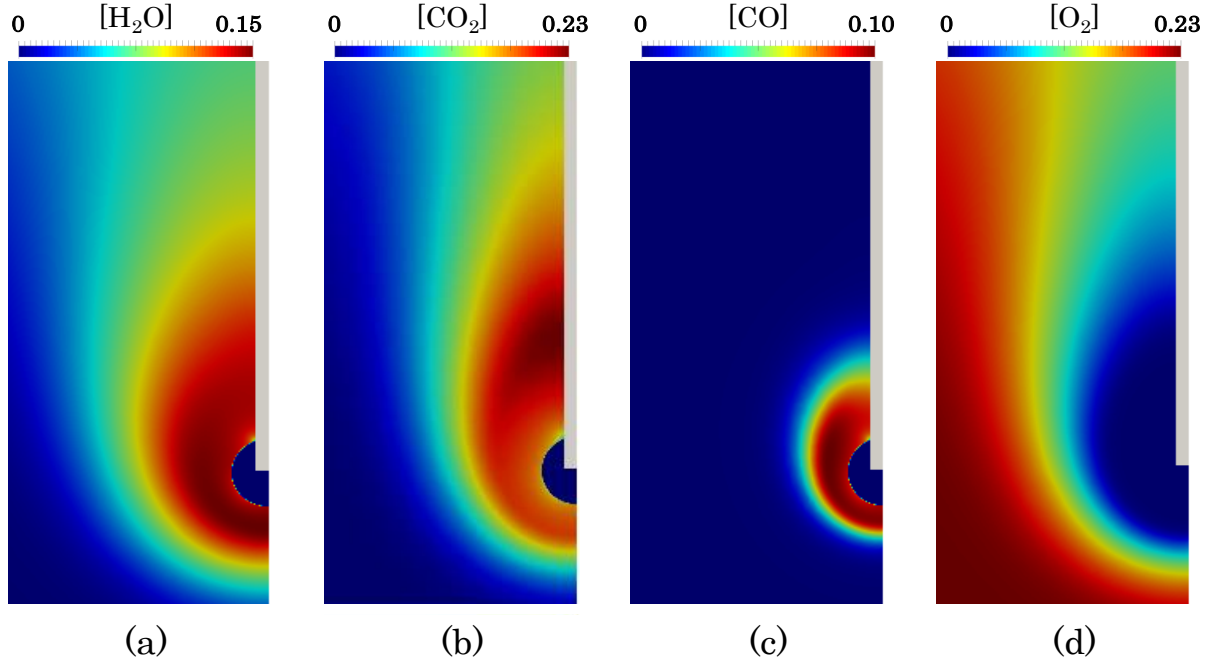


Figure 5: Case 2: 2D maps of H_2O (a), CO_2 (b), CO (c), O_2 (d) mass fractions. The gray region represents the fiber. Time $t = 0.67$ s.

$$\omega_k = \sum_i^{N_s} \omega_i N_{k,i} \frac{M_{w,k}}{M_{w,i}} \quad (29)$$

where $N_{k,i}$ is the number of atoms k in species i . The mixture fraction Z is defined as:

$$Z = \frac{\beta - \beta_{ox}}{\beta_{fuel} - \beta_{ox}} \quad (30)$$

The fuel composition used to calculate β_{fuel} is the gaseous composition at the droplet interface, including the dilution with the surrounding species. Therefore, Z assumes value 1 on the interface and 0 in the pure oxidizer. The stoichiometric Z_{st} is easily calculated imposing $\beta = 0$ (whatever the chemical reactions involved):

$$Z_{st} = -\frac{\beta_{ox}}{\beta_{fuel} - \beta_{ox}} \quad (31)$$

The Z_{st} isocontour is evidenced in Figure 4. It is colored by the local scalar dissipation rate χ :

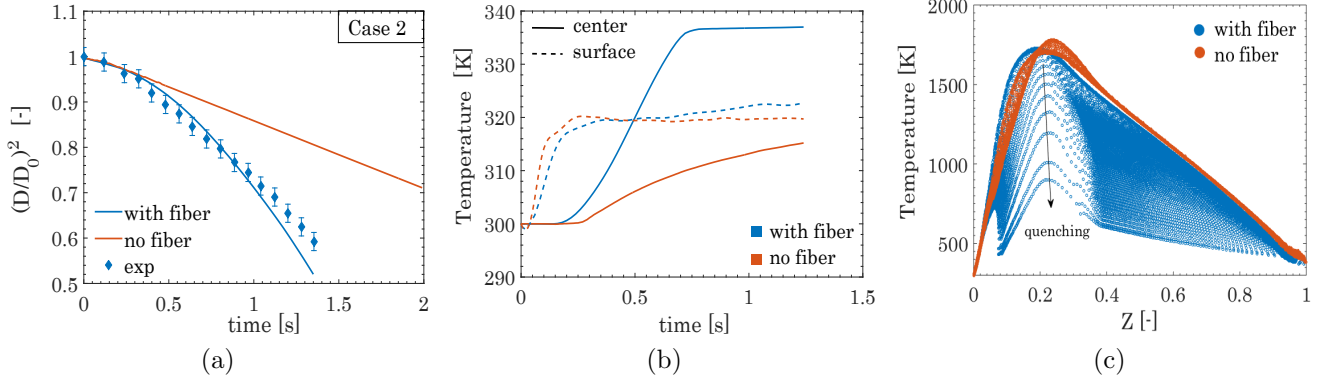


Figure 6: Effect of the fiber (Case 2): $(D/D_0)^2$ plot (a), droplet temperature (b) and T - Z scatterplot at $t = 0.67$ s (c). Experimental data from [23].

$$\chi = 2\mathcal{D}_{N_2}|\nabla Z|^2 \quad (32)$$

The inverse of $|\nabla Z|^2$ is proportional to the flame thickness [58]. As can be seen in Figure 4, the lower part of the flame is thinner because it behaves similarly to a counterflow flame: the Stefan flow generated by the droplet vaporization is opposed to the upward flow due to buoyancy, tending to bring Z iso-surfaces closer and reducing the thickness of the reactive region. As a consequence, the highest concentration of radical species (OH , H , HO_2) are localized in this region. The flame becomes thicker in the upper part of the flame because of the absence of a significant relative velocity component normal to the Z iso-surfaces.

5.3. The thermal effect of the fiber

The temperature of the fiber increases due to the vicinity of the flame (up to ~ 850 K, Figure 4c) and this is known to affect the combustion process [14], creating a preferential path for the heat flux on the droplet (especially for large fiber diameters). In order to quantify the thermal perturbation caused by the fiber, Case 2 has also been simulated considering it as adiabatic. Figure 6a shows that if the fiber heat transfer is neglected the model is not able to predict the correct diameter decay, since the burning rate is strongly underestimated. In particular, two main processes govern the liquid temperature (Figure 6b): initially, after a slight decrease of T due to evaporation, the droplet surface receives heat from the flame, releasing vapor in the gas-

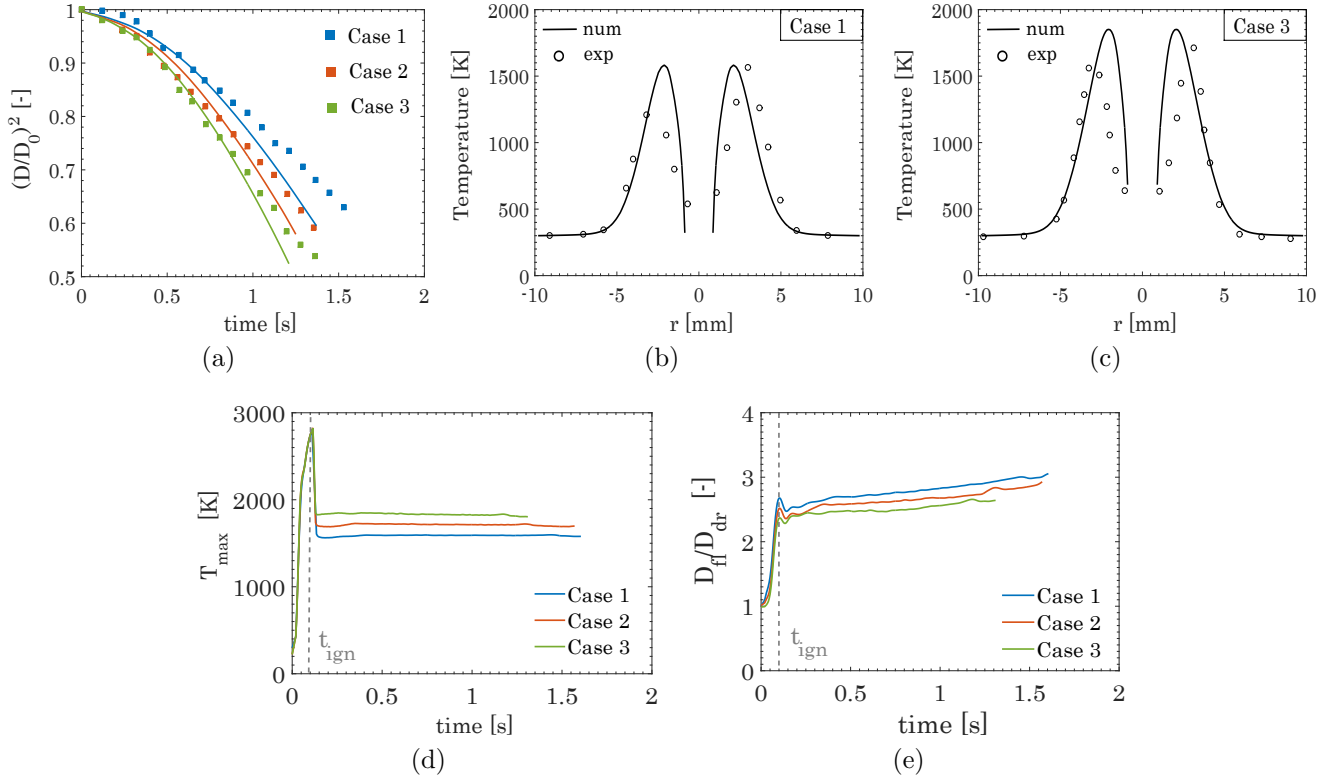


Figure 7: Effect of oxygen: $(D/D_0)^2$ plot of Cases 1, 2, 3 (a) and radial T profiles of Cases 1 (b) and 3 (c) at $t = 0.67$ s. Profiles of flame temperature T_{max} (d) and standoff ratio D_{fl}/D_{dr} (e) over time. Experimental data from [23].

phase and rapidly reaching an equilibrium temperature (i.e. wet-bulb temperature ~ 320 K). In the meantime the fiber temperature increases, conducting heat directly inside the liquid. Since evaporation is not possible inside the droplet, the temperature rapidly increases and reaches the boiling temperature T_b in the center. The evaporation rate evaluation switches to the boiling model (Table 1) and the temperature remains constant and equal to T_b (blue solid line in Figure 6b). This creates a situation in which the liquid surface evaporates at $T < T_b$, while the droplet interior boils ($T = T_b$).

At the initial stages the heat absorbed from the droplet surface governs the vaporization while the fiber plays a major role towards the end of the simulation (when the fiber is hotter and the droplet smaller), mainly affecting the internal temperature. If the fiber (Equation 17) and the boiling (Equation 22) are accounted for, the model predicts the burning rate (Figure 6a) with a reasonable accuracy.

Another interesting effect of the fiber is the partial quenching of the flame (Figure 4) close to

the fiber surface, due to its thermal inertia. In Figure 6c a scatterplot of the temperature with respect to the passive scalar Z (Equation 30) is reported, showing a wide quenching region when the fiber is accounted for. Focusing on the $Z_{st} \sim 0.21$, the flame temperature decreases of ~ 1000 K approaching the fiber providing an incomplete combustion in this region. This effect is of primary importance since it leads to an accumulation of radicals and partial oxidation products at the fiber surface.

5.4. *The effect of the oxygen concentration*

In Figure 7a the numerical diameter decays of Cases 1, 2, 3 are presented and compared with the experiments. The numerical results have been shifted, so that time $t = 0$ represents the ignition time. The agreement is satisfactory, within the uncertainties of the experimental data. The explanation for the differences in the diameter decay is straightforward: increasing the oxygen concentration leads to a higher temperature of (i) the flame and thus (ii) of the fiber. Both induce a more intense vaporization of the liquid, increasing the burning rate and diminishing the droplet lifetime. The maximum temperature profile over time is reported in Figure 7d: after the ignition the flame temperature stabilizes at a constant value, which is higher for higher oxygen concentrations in the gas-phase. This can also be observed from the radial temperature profiles, taken along an horizontal line passing through the droplet center (for Cases 1, 3 in Figures 7b, 7c). The model predicts the experimental data with a reasonable accuracy, considering the error associated with the measurements (up to $\sim 10\%$, as reported in [23]). Experimental errors can also be seen in the slight asymmetry of the temperature profiles. The difference in the maximum flame temperatures is ~ 150 K, with the peak for Case 3 slightly closer to the droplet surface. As reported in the last section of this paper, the agreement with the experimental results concerning the radial temperature profile improves including water condensation on the droplet surface.

Finally, it is worth analyzing the flame position with respect to the droplet interface (standoff ratio) for the three cases (Figure 7e). The flame diameter D_{fl} is indicated in Figure 4 (c) and corresponds to the maximum horizontal distance of the Z_{st} isoline from the symmetry axis. The flame position with respect to the droplet surface slightly increases over time for all the three cases. The flame approaches the droplet surface increasing the oxygen concentration, since the

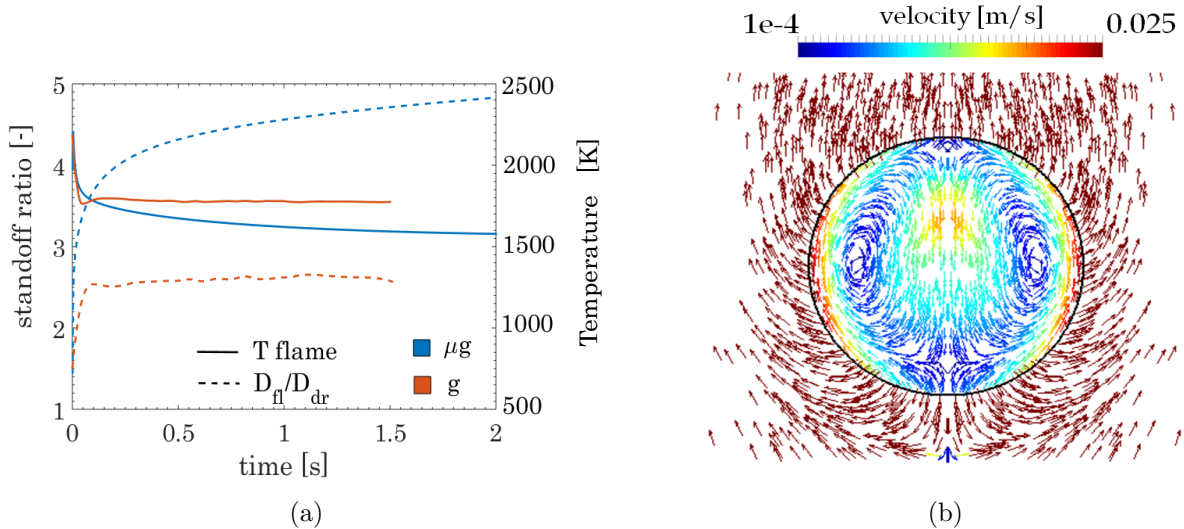


Figure 8: Case 2: profiles of flame T and relative flame position D_{fl}/D_{dr} (standoff ratio) in microgravity and normal gravity (a). Two-phase velocity field around and inside the droplet (b), time $t=1$ s.

stoichiometric condition at Z_{st} is satisfied closer to the droplet. The vicinity of the flame further increases the vaporization rate from the droplet, further enhancing the effect of the higher oxygen concentration. This is in agreement to what observed by other authors [60, 61].

5.5. The effect of gravity

The presence of a gravity field creates an upward buoyant flow ($v_{max} \sim 0.4$ m/s) once the flame is ignited and stabilized, which significantly influences the droplet combustion physics. The external convection forms a thin boundary layer which significantly affects the heat and mass transport rates. To better discuss and highlight the effects of gravity, we simulated the cases in Table 3 in microgravity conditions (μg), imposing $\mathbf{g} = \mathbf{0}$. The results are compared with the cases simulated in normal gravity in terms of flame temperature, standoff ratio (D_{fl}/D_{dr}), flame geometry and internal motion. The presence of external convection influences:

- *The droplet shape*: under a convective field the droplet geometry is no longer spherical, due to the deformation induced by the flow. On principle this can affect the vaporization rate, since the surface area available for the vaporization is different. However, we noticed that for small droplets this is usually a minor effect [21] and that the sphericity coefficient ~ 1 for most of the cases of our interest;

- *The flame geometry:* in microgravity the flame is spherical and its distance from the droplet increases after the ignition, reaching a value of ~ 4 -5 times the droplet diameter (Figure 8 a). As a consequence the flame temperature decreases, providing a possible radiative extinction if the flame diameter is large enough [8]. On the other hand, in normal gravity the flame is axisymmetric and much closer to the droplet, maintaining its relative position almost constant in time (it is actually slightly increasing). This is due to the convective transfer of oxygen to the reactive region (much faster than pure diffusion), which satisfies the stoichiometric requirement of the flame front at a shorter distance. The average flame thickness is significantly reduced, especially in the lower part of the flame.

As a result, the flame temperature is practically constant in time and higher than the case in microgravity (of ~ 250 K). Moreover, the flame further approaches the droplet surface when the oxygen concentration increases. We found this effect to be similar both in microgravity and normal gravity, indicating that the presence of convection does not significantly affect the response of the flame distance to the oxygen concentration;

- *The internal circulation:* in microgravity the heat transfer in the liquid phase is mainly governed by conduction due to the absence of internal motion. When gravity is present, the buoyancy-driven convection induces an internal motion in the liquid phase (shear stress continuity) which significantly enhances the internal heat transfer [62]. Figure 8 (b) shows the two-phase velocity field for the burning droplet, highlighting the internal motion. As reported by many authors [2], the internal flow can be approximated as a Hill's vortex, having a toroidal core region within the droplet. The maximum velocity in the liquid phase (~ 2.5 cm/s) is an order of magnitude less than the relative gas-phase velocity (~ 30 cm/s), in agreement to what observed by Prakash and Sirignano [63].

It is worth noticing that the gas-phase velocity field exhibits a significant radial flow at the interface, due to the Stefan flow induced by the vaporization. Several authors observed that this radial flow leads to a significant reduction of the drag coefficient on the droplet [64, 65], due to the expansion of the gas-phase boundary layer which significantly reduces the viscous force on the droplet. As an additional effect, this can make the liquid velocity field much less

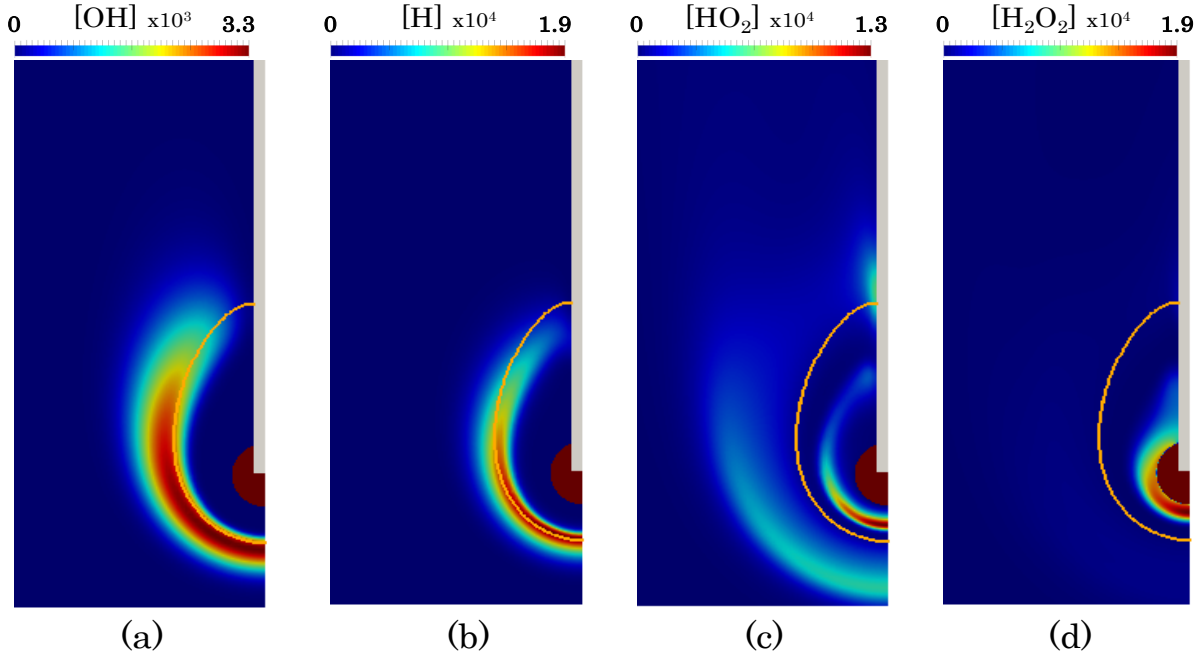


Figure 9: Case 2: 2D maps of OH (a), H (b), HO₂ (c), H₂O₂ (d) mass fractions. The orange solid line is the flame front (Z_{st}), the red region is the droplet. Time $t = 0.67$ s.

sensitive to the external convection, reducing the intensity of the internal motion. Following a fairly complex theoretical analysis, Sadhal [66] observes that in the limit of extremely high radial flows the internal toroidal structure can be totally destroyed, due to the absence of a tangential component of the relative gas-phase velocity at the interface.

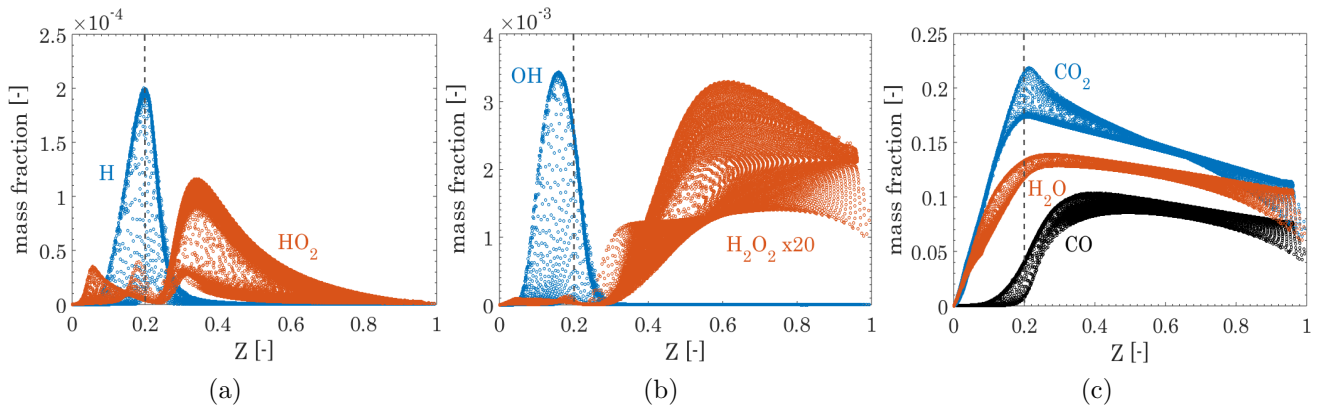


Figure 10: Case 2: ω_i - Z scatterplots of main species mass fractions at time $t = 0.67$ s.

5.6. Distribution of the species in the gas phase

Once a passive scalar Z is defined (Equation 30), we can analyze the main species distribution (for Case 2 at $t = 0.67$ s) along the flame coordinate. The results are reported in Figures 9 and 10, highlighting the Z_{st} . In order to analyze the rate of production of the species in a simpler system, a 1D counterflow diffusion flame has been simulated with `OpenSMOKE++` [43], replicating the same conditions encountered in the droplet flame (in terms of χ , geometry, inlet T and composition). As already reported, most of the species have a peak in the high scalar dissipation rate (χ) region (low thickness), the lower part of the flame (Figure 9). The OH radical is slightly below the Z_{st} due to the need of O_2 for its formation, while the H radical peak is at Z_{st} . The HO_2 radical shows an interesting profile, with three peaks along Z : on the rich side, HO_2 is mainly produced by $O_2 + CH_2OH \rightarrow HO_2 + CH_2O$, while on the lean side $H + O_2 + (M) \rightarrow HO_2 + (M)$ is dominant, due to the high diffusivity of H which escapes the flame front. The intermediate HO_2 peak is due to the flame quenching at the fiber surface (clearly visible in the HO_2 mass fraction map in Figure 9c), which decreases the temperature and stabilizes HO_2 . The important presence of HO_2 for $Z > Z_{st}$ is also responsible for the hydrogen peroxide H_2O_2 formation (Figure 10b) through the abstraction reaction $HO_2 + CH_3OH \rightarrow H_2O_2 + CH_2OH$, extensively investigated by other authors [67, 68]. At $Z < Z_{st}$, OH recombination reaction ($2OH \rightarrow H_2O_2$) is the main responsible for H_2O_2 formation in the lean region. At $Z \sim 0.35$ there is an intermediate peak (not clearly visible due to the very low concentration), still due to the flame quenching at the fiber which locally cools the flame. The main combustion products are H_2O and CO_2 (Figure 10c), while CO is almost completely oxidized by OH at the flame front. With respect to the case without fiber, we notice a lower concentration of these species. It is worth noticing that CO, CO_2 and H_2O are present in significant amount at the droplet interface ($Z = 1$), because of back diffusion from the flame. Differently from CO and CO_2 , water can condense on the droplet surface due to the low interface temperature (~ 320 K). This will be analyzed in the next section.

5.7. Absorption of water in the liquid phase

The water present among the combustion products in the gas-phase is miscible with methanol and it can condense on the droplet surface. If the liquid temperature is sufficiently high, water

starts vaporizing as well and a two-component thermodynamics is established. This has been widely investigated in recent numerical and experimental works regarding alcohol combustion [69, 70, 61]. From the modeling point of view only few things change:

- The species equation must be solved also for the liquid phase. The only difference is that a source term \dot{m}_i has to be included to account for the amount of species i lost at the liquid interface for evaporation ($\dot{m}_i < 0$) or added by condensation ($\dot{m}_i > 0$):

$$\frac{\partial \rho \omega_i^L}{\partial t} + \nabla \cdot (\rho \mathbf{v} \omega_i^L) = -\nabla \cdot \mathbf{j}_i^L + \dot{m}_i \quad (33)$$

The equation for the gas-phase remains Equation 6. The diffusion coefficients \mathcal{D}_i in the liquid phase (needed for the flux \mathbf{j}_i^L) are computed with the Leffler-Cullinan approach [71].

- The boiling temperature T_b is needed to trigger the boiling sub-model (Table 1). In a two-component mixture (water and methanol) T_b depends on the local composition and it should be calculated in every point in the liquid phase at every time step. This can be a very expensive procedure, since finding T_b involves the solution of a non-linear algebraic equation (Equation 8). It is much easier to adopt the local boiling pressure p_b :

$$\dot{m} = \begin{cases} \frac{\sum_i^{N_{s,L}} \mathbf{j}_i}{1 - \sum_i^{N_{s,L}} \omega_i} \nabla \alpha, & \text{if } p > p_b \\ -\frac{\rho C_p \frac{\partial T}{\partial t}}{\Delta h_{ev}}, & \text{if } p \leq p_b \end{cases} \quad (34)$$

and similarly:

$$\dot{m}_i = \begin{cases} \mathbf{j}_i \nabla \alpha + \dot{m} \omega_i & \text{if } p > p_b \\ \dot{m} \frac{p_i^0(T)}{p} x_i \frac{M_{w,i}}{M_w} \gamma_i & \text{if } p \leq p_b \end{cases} \quad (35)$$

where the boiling pressure p_b can be directly calculated in every point of the liquid phase as:

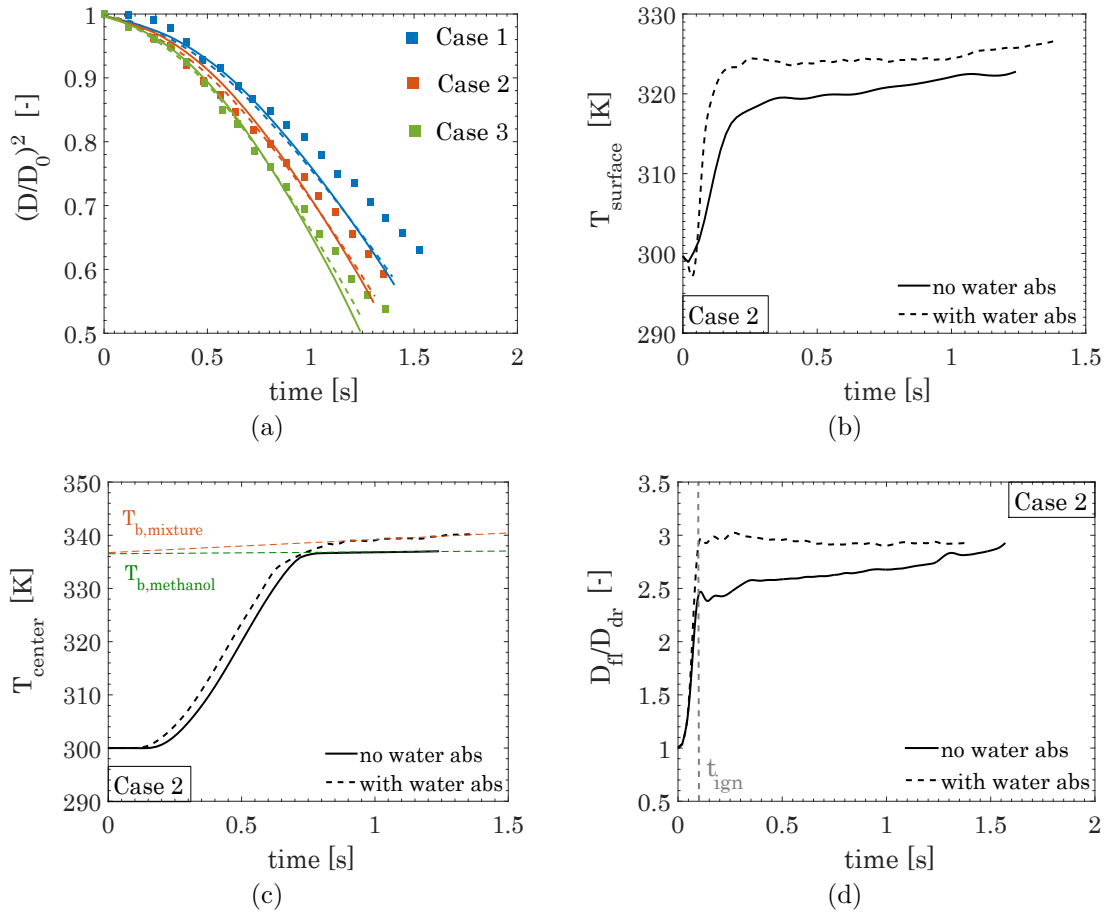


Figure 11: Effect of condensed water: $(D/D_0)^2$ plot of Cases 1, 2, 3 (a), surface temperature profiles (b), internal temperature profiles (c) and standoff ratio D_{ff}/D_{dr} profiles (d) of Case 2.

$$p_b = \sum_i^{Ns_L} p_i^0(T) x_i \gamma_i \quad (36)$$

In order to highlight the effect of the absorbed water on the droplet combustion, we simulated the three cases in Table 3 including the water condensation flux. This is done by simply initializing the initial fuel composition with a small amount of water ($\omega_0^L = 10^{-4}$ in this case). The results are reported in Figure 11.

Referring to Figure 11a, we can identify two main vaporization regimes of the methanol-water mixture. During the first period the droplet is consumed faster when water absorption is accounted for: this happens because of the condensation heat released on the surface, which increases the temperature ($\sim 4-5$ K). Since methanol is (initially) the main component of the two-phase mixture, it vaporizes faster [69]. This can be clearly seen in Figure 11b, where the surface temperatures for the two cases are reported. Later on, the amount of condensed water becomes significant and the droplet global vaporization rate is retarded (also because of methanol dilution). This effect seems to be more enhanced at high temperatures (Case 3) due to the higher water concentration in the gas-phase. Moreover, the water absorbed at the surface is transported (by diffusion and internal convection) inside the liquid phase, close to the fiber. The vaporization enthalpy of the methanol-water mixture locally increases ($\Delta h_{ev,water} > \Delta h_{ev,meth}$) and the internal boiling flux is diminished (Equation 22), further slowing the vaporization rate. At the droplet center the boiling conditions are reached for both cases ($T = T_b$, Figure 11c). While T_b is constant for pure methanol vaporization, it constantly increases for the mixture because of water absorption ($T_{b,water} > T_{b,meth}$) which changes the liquid composition. It is also worth analyzing the difference in the flame position with respect to the droplet surface (Figure 11d). The standoff ratio is higher due to the more intense methanol vaporization which pushes the flame farther. This is reflected by the comparison of the radial temperature profiles (previously shown in Figure 7 b,c) in Figures 12(a,b): when water absorption is included, the temperature maximum slightly shifts away from the droplet and improves the agreement with the experimental data. Lee and Law [69] also report the existence of a final evaporation stage in which the condensed water starts to vaporize again once reached a significant concentration in the liquid. However, we did not notice this phenomena

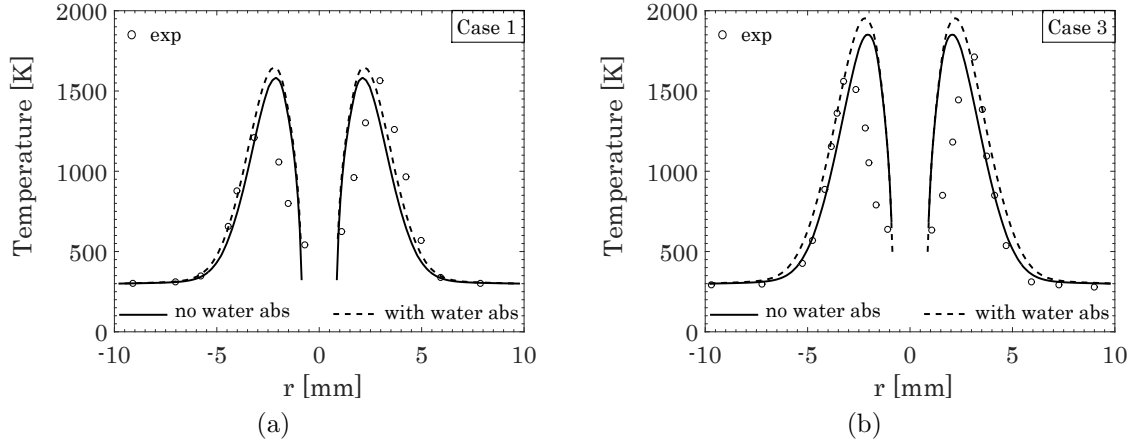


Figure 12: Effect of condensed water: radial temperature profiles for Case 1 (a) and Case 3 (b).

in our case probably because of the relatively low amount of water absorbed. In particular, we noticed less than 10% (in mass) of water accumulation in the liquid phase at the end of the simulation (for all the cases). We found this effect to be negligible on the diameter decay (Figure 11a), since the vaporization rate is controlled by the internal boiling (mainly methanol) induced by the fiber.

6. Conclusions

In this paper we presented a CFD computational framework for the numerical modeling of the combustion of suspended fuel droplets in normal gravity, accounting for: (i) the efficient numerical management of the gas-phase combustion through the operator-splitting approach (as well as a radiation model), (ii) a multiregion approach to model the thermal perturbation of the fiber, (iii) a vaporization model which includes the possibility of boiling in the liquid phase. The numerical model has been adopted to simulate the combustion of suspended methanol droplets from a recent experimental work. The agreement with the experimental data was satisfactory, both in terms of diameter decay and radial temperature profiles. In particular:

- The thermal perturbation of the fiber strongly affects the vaporization rate, conducting heat inside the liquid phase. The droplet interior is subjected to boiling, while the external surface evaporates by diffusion. A partial quenching of the flame occurs close to its surface, accumulating oxidized species;

- Higher oxygen concentrations increase the flame temperature, bring the flame closer to the droplet surface and diminishes the droplet lifetime;
- The presence of a buoyant flow provides an axisymmetric flame geometry, with a lower standoff ratio and a higher flame temperature if compared to microgravity. Furthermore, the shear stress at the interface induces an circulation in the liquid phase, which enhances the internal heat transfer;
- The flame is thinner in the lower part of the droplet (high χ), where we found the peak of most of the radical species. A brief analysis of the distribution of species in the gas phase shed light on the chemical behavior of H and HO₂ radicals and on the quenching effect at the fiber;
- The water produced in the gas-phase condenses on the droplet surface, with two main effects: (i) an initial increase of the burning rate, due to the release of the condensation enthalpy at the droplet surface and (ii) a subsequent delay, because of water accumulation. The effect on the diameter decay is negligible, while the comparison of the radial temperature profiles slightly improves.

Further works will be focused on the combustion modeling of more complex fuels (such as n-alkanes and multicomponent fuels), investigating additional phenomena such as cool flames, soot formation and preferential vaporization.

Acknowledgments

We acknowledge the CINECA award under the ISCRA initiative, for the availability of high performance computing resources and support (ISCRA-B: HP10BGXWCZ).

Appendix A. Grid refinement analysis

The sensitivity of the numerical results with respect to the mesh size is investigated in this appendix. Case 2 (Table 3) is simulated at three increasing levels of refinement: n=1 (37,000 cells), n=2 (92,000 cells) and n=3 (160,000 cells). The mesh is refined only in the fluid region,

Variable	Refinement levels			∞	O
	n=1	n=2	n=3		
T_{flame}	1711.29	1760.2	1759.95	1759.83	2.2
T_{surface}	316.36	319.21	319.24	319.25	2.3
CO_{max}	0.109	0.118	0.117	0.1165	1.8
$\text{CO}_{2,\text{max}}$	0.248	0.236	0.234	0.233	1.8
$\text{H}_2\text{O}_{\text{max}}$	0.171	0.146	0.143	0.142	2.3
OH_{max}	0.00311	0.00373	0.00364	0.0036	1.7

Table A.4: Grid refinement analysis for Case 2 at three different levels of resolution. The reference value ∞ is estimated through Richardson extrapolation. The approximate order of convergence O is also reported.

maintaining the proportions between the fine region (around the droplet) and the coarser one (outside the droplet). The analysis is made in terms of the variables reported in Table A.4 at time $t = 0.5$ s. The values are compared with the continuum value at zero grid spacing, evaluated adopting the Richardson extrapolation [72]. The approximate orders of convergence are also calculated.

The code shows convergence orders between 1.7 and 2.3 for the examined variables. Even though n=3 is the most accurate case, the refinement level n=2 (92,000 cells) has been used in this work, since the computational time is significantly reduced. Adopting this resolution, the average error for the reported variables remains between 0.01% and 2%.

Nomenclature

Acronyms

VOF Volume Of Fluid

Greek letters

α VOF marker function $[-]$

β thermal expansion coefficient $[\frac{1}{K}]$

χ scalar dissipation rate $[s^{-1}]$

ΔH_R enthalpy of reaction $[J/kg]$

Δh_{ev}	evaporation enthalpy $\left[\frac{J}{kg}\right]$
δ_s	Dirac delta $\left[\frac{1}{m}\right]$
γ	activity coefficient $[-]$
$\hat{\phi}$	mixture gas-phase fugacity coefficient $[-]$
κ	curvature $\left[\frac{1}{m}\right]$
μ	dynamic viscosity $\left[\frac{kg}{ms}\right]$
ν	stoichiometric coefficient $[-]$
ω	mass fraction $[-]$
ϕ	pure gas-phase fugacity coefficient $[-]$
ψ	generic variable
ρ	density $\left[\frac{kg}{m^3}\right]$
σ	surface tension $\left[\frac{N}{m}\right]$

Roman letters

\dot{m}	evaporation flux $\left[\frac{kg}{m^2s}\right]$
\dot{q}	heat flux per unit volume $\left[\frac{W}{m^3}\right]$
\mathcal{D}	mass diffusion coefficient $\left[\frac{m^2}{s}\right]$
\mathbf{f}	force per unit volume $\left[\frac{N}{m^3}\right]$
\mathbf{j}	diffusion flux $\left[\frac{kg}{m^2s}\right]$
S	source term
T	transport term

\mathbf{v}	velocity $\left[\frac{m}{s}\right]$
\mathbf{x}	position vector $[m]$
a_p	absorption coefficient $[-]$
C_p	constant pressure specific heat $\left[\frac{J}{kgK}\right]$
D	diameter $[m]$
H	height of the mesh $[m]$
k	thermal conductivity $\left[\frac{W}{mK}\right]$
L	base radius of the mesh $[m]$
M_w	molecular weight $\left[\frac{kg}{mol}\right]$
N_s	Number of species $[-]$
p	pressure $[Pa]$
p^0	vapor pressure $[Pa]$
p_{rgh}	dynamic pressure $[Pa]$
R	reaction rate $\left[\frac{kg}{m^3s}\right]$
r	radius $[m]$
t	time $[s]$
T	temperature $[K]$
v	molar volume $\left[\frac{m^3}{mol}\right]$
x	liquid mole fraction $[-]$
y	gas mole fraction $[-]$

Z mixture fraction [-]

Subscripts

0 initial, reference

b boiling

env ambient

f fiber

G gas

i i -th species

j j -th reaction

L liquid

rad radiative

s solid

References

References

- [1] G. Tryggvason, R. Scardovelli, S. Zaleski, Direct numerical simulations of gas–liquid multi-phase flows, Cambridge University Press, 2011.
- [2] W. A. Sirignano, Fluid dynamics and transport of droplets and sprays, Cambridge university press, 1999.
- [3] S. Okajima, S. Kumagai, Further investigations of combustion of free droplets in a freely falling chamber including moving droplets, in: Proceedings of the Combustion Institute, Vol. 15, Elsevier, 1975, pp. 401–407.

- [4] D. L. Dietrich, J. B. Haggard Jr, F. L. Dryer, V. Nayagam, B. D. Shaw, F. A. Williams, Droplet combustion experiments in spacelab, in: Proceedings of the Combustion Institute, Vol. 26, Elsevier, 1996, pp. 1201–1207.
- [5] A. J. Marchese, F. L. Dryer, V. Nayagam, Numerical modeling of isolated n-alkane droplet flames: initial comparisons with ground and space-based microgravity experiments, Combustion and Flame 116 (3) (1999) 432–459.
- [6] A. Cuoci, M. Mehl, G. Buzzi-Ferraris, T. Faravelli, D. Manca, E. Ranzi, Autoignition and burning rates of fuel droplets under microgravity, Combustion and Flame 143 (3) (2005) 211–226.
- [7] T. I. Farouk, F. L. Dryer, Isolated n-heptane droplet combustion in microgravity: cool flames–two-stage combustion, Combustion and Flame 161 (2) (2014) 565–581.
- [8] A. Cuoci, A. E. Saufi, A. Frassoldati, D. L. Dietrich, F. A. Williams, T. Faravelli, Flame extinction and low-temperature combustion of isolated fuel droplets of n-alkanes, Proceedings of the Combustion Institute 36 (2) (2017) 2531–2539.
- [9] D. C. K. Rao, S. Syam, S. Karmakar, R. Joarder, Experimental investigations on nucleation, bubble growth, and micro-explosion characteristics during the combustion of ethanol/jet a-1 fuel droplets, Experimental Thermal and Fluid Science 89 (2017) 284–294.
- [10] M. A. Pfeil, L. J. Groven, R. P. Lucht, S. F. Son, Effects of ammonia borane on the combustion of an ethanol droplet at atmospheric pressure, Combustion and flame 160 (10) (2013) 2194–2203.
- [11] C. Chauveau, I. Gökalp, D. Segawa, T. Kadota, H. Enomoto, Effects of reduced gravity on methanol droplet combustion at high pressures, Proceedings of the Combustion Institute 28 (1) (2000) 1071–1077.
- [12] C. Chauveau, B. Vieille, I. Gökalp, D. Segawa, T. Kadota, A. Nakainkyo, Effects of gravitational acceleration on high pressure combustion of methanol droplets, Journal de Chimie Physique et de Physico-Chimie Biologique 96 (6) (1999) 1031–1037.

- [13] B. Shaw, J. Wei, Combustion of methanol droplets in air-diluent environments with reduced and normal gravity, *Journal of Combustion* 2012.
- [14] C. Chauveau, F. Halter, A. Lalonde, I. Gokalp, An experimental study on the droplet vaporization: effects of heat conduction through the support fiber, in: *Proc. of 22 nd Annual Conference on Liquid Atomization and Spray Systems (ILASS Europe 2008)*, Vol. 59, 2008, p. 61.
- [15] R. Banerjee, Numerical investigation of evaporation of a single ethanol/iso-octane droplet, *Fuel* 107 (2013) 724–739.
- [16] O. A. George, J. Xiao, C. S. Rodrigo, R. Mercadé-Prieto, J. Sempere, X. D. Chen, Detailed numerical analysis of evaporation of a micrometer water droplet suspended on a glass filament, *Chemical Engineering Science* 165 (2017) 33–47.
- [17] Y. Wang, X. Chen, X. Wang, V. Yang, Vaporization of liquid droplet with large deformation and high mass transfer rate, ii: Variable-density, variable-property case, *Journal of Computational Physics* 394 (2019) 1–17.
- [18] B. Wang, A. Kronenburg, G. L. Tufano, O. T. Stein, Fully resolved DNS of droplet array combustion in turbulent convective flows and modelling for mixing fields in inter-droplet space, *Combustion and Flame* 189 (2018) 347–366.
- [19] Y. Jin, B. Shaw, Computational modeling of n-heptane droplet combustion in air-diluent environments under reduced-gravity, *International Journal of Heat and Mass Transfer* 53 (25-26) (2010) 5782–5791.
- [20] N. Ghata, B. D. Shaw, Computational modeling of unsupported and fiber-supported n-heptane droplet combustion in reduced gravity: a study of fiber effects, *Combustion Science and Technology* 187 (1-2) (2015) 83–102.
- [21] A. Saufi, A. Frassoldati, T. Faravelli, A. Cuoci, DropletSMOKE++: A comprehensive multiphase CFD framework for the evaporation of multidimensional fuel droplets, *International Journal of Heat and Mass Transfer* 131 (2019) 836–853.

- [22] A. Saufi, R. Calabria, F. Chiariello, A. Frassoldati, A. Cuoci, T. Faravelli, P. Massoli, An experimental and CFD modeling study of suspended droplets evaporation in buoyancy driven convection, *Chemical Engineering Journal* (2019) 122006.
- [23] A. K. Yadav, A. Chowdhury, A. Srivastava, Interferometric investigation of methanol droplet combustion in varying oxygen environments under normal gravity, *International Journal of Heat and Mass Transfer* 111 (2017) 871–883.
- [24] C. W. Hirt, B. D. Nichols, Volume of fluid (VOF) method for the dynamics of free boundaries, *Journal of computational physics* 39 (1) (1981) 201–225.
- [25] J. Roenby, H. Bredmose, H. Jasak, A computational method for sharp interface advection, *Royal Society open science* 3 (11) (2016) 160405.
- [26] S. S. Deshpande, L. Anumolu, M. F. Trujillo, Evaluating the performance of the two-phase flow solver interfoam, *Computational science & discovery* 5 (1) (2012) 014016.
- [27] R. B. Bird, Transport phenomena, *Applied Mechanics Reviews* 55 (1) (2002) R1–R4.
- [28] J. M. Smith, Introduction to chemical engineering thermodynamics, ACS Publications, 1950.
- [29] J. Brackbill, D. B. Kothe, C. Zemach, A continuum method for modeling surface tension, *Journal of computational physics* 100 (2) (1992) 335–354.
- [30] S. Popinet, An accurate adaptive solver for surface-tension-driven interfacial flows, *Journal of Computational Physics* 228 (16) (2009) 5838–5866.
- [31] A. Albadawi, D. Donoghue, A. Robinson, D. Murray, Y. Delauré, Influence of surface tension implementation in volume of fluid and coupled volume of fluid with level set methods for bubble growth and detachment, *International Journal of Multiphase Flow* 53 (2013) 11–28.
- [32] A. Q. Raeini, M. J. Blunt, B. Bijeljic, Modelling two-phase flow in porous media at the pore scale using the volume-of-fluid method, *Journal of Computational Physics* 231 (17) (2012) 5653–5668.

- [33] R. P. Fedkiw, T. Aslam, B. Merriman, S. Osher, A non-oscillatory eulerian approach to interfaces in multimaterial flows (the ghost fluid method), *Journal of computational physics* 152 (2) (1999) 457–492.
- [34] V. Vukčević, H. Jasak, I. Gatin, Implementation of the ghost fluid method for free surface flows in polyhedral finite volume framework, *Computers & Fluids* 153 (2017) 1–19.
- [35] S. J. Cummins, M. M. Francois, D. B. Kothe, Estimating curvature from volume fractions, *Computers & structures* 83 (6-7) (2005) 425–434.
- [36] E. Marchandise, P. Geuzaine, N. Chevaugeon, J.-F. Remacle, A stabilized finite element method using a discontinuous level set approach for the computation of bubble dynamics, *Journal of Computational Physics* 225 (1) (2007) 949–974.
- [37] O. Desjardins, V. Moureau, H. Pitsch, An accurate conservative level set/ghost fluid method for simulating turbulent atomization, *Journal of Computational Physics* 227 (18) (2008) 8395–8416.
- [38] S. Popinet, Numerical models of surface tension, *Annual Review of Fluid Mechanics* 50 (2018) 49–75.
- [39] J. Palmore Jr, O. Desjardins, A volume of fluid framework for interface-resolved simulations of vaporizing liquid-gas flows, *Journal of Computational Physics* 399 (2019) 108954.
- [40] T. Harada, H. Watanabe, Y. Suzuki, H. Kamata, Y. Matsushita, H. Aoki, T. Miura, A numerical investigation of evaporation characteristics of a fuel droplet suspended from a thermocouple, *International Journal of Heat and Mass Transfer* 54 (1-3) (2011) 649–655.
- [41] J.-R. Yang, S.-C. Wong, On the discrepancies between theoretical and experimental results for microgravity droplet evaporation, *International Journal of Heat and Mass Transfer* 44 (23) (2001) 4433–4443.
- [42] C. Chauveau, M. Birouk, F. Halter, I. Gökalp, An analysis of the droplet support fiber effect

- on the evaporation process, *International Journal of Heat and Mass Transfer* 128 (2019) 885–891.
- [43] A. Cuoci, A. Frassoldati, T. Faravelli, E. Ranzi, OpenSMOKE++: An object-oriented framework for the numerical modeling of reactive systems with detailed kinetic mechanisms, *Computer Physics Communications* 192 (2015) 237–264.
- [44] C. L. Yaws, *The Yaws Handbook of Physical Properties for Hydrocarbons and Chemicals: Physical Properties for More Than 54,000 Organic and Inorganic Chemical Compounds, Coverage for C1 to C100 Organics and Ac to Zr Inorganics*, Gulf Professional Publishing, 2015.
- [45] R. C. Reid, J. M. Prausnitz, B. E. Poling, *The properties of gases and liquids*.
- [46] A. Fredenslund, R. L. Jones, J. M. Prausnitz, Group-contribution estimation of activity coefficients in nonideal liquid mixtures, *AIChE Journal* 21 (6) (1975) 1086–1099.
- [47] G. Strang, On the construction and comparison of difference schemes, *SIAM journal on numerical analysis* 5 (3) (1968) 506–517.
- [48] A. Cuoci, A. Frassoldati, T. Faravelli, E. Ranzi, A computational tool for the detailed kinetic modeling of laminar flames: Application to C₂H₄/CH₄ coflow flames, *Combustion and Flame* 160 (5) (2013) 870–886.
- [49] C. J. Greenshields, *OpenFOAM user guide*, OpenFOAM Foundation Ltd, version 3 (1).
- [50] P. S. Veloo, Y. L. Wang, F. N. Egolfopoulos, C. K. Westbrook, A comparative experimental and computational study of methanol, ethanol, and n-butanol flames, *Combustion and Flame* 157 (10) (2010) 1989–2004.
- [51] E. Ranzi, A. Sogaro, P. Gaffuri, G. Pennati, T. Faravelli, A wide range modeling study of methane oxidation, *Combustion science and technology* 96 (4-6) (1994) 279–325.

- [52] W. K. Metcalfe, S. M. Burke, S. S. Ahmed, H. J. Curran, A hierarchical and comparative kinetic modeling study of C1- C2 hydrocarbon and oxygenated fuels, *International Journal of Chemical Kinetics* 45 (10) (2013) 638–675.
- [53] S. M. Burke, U. Burke, R. Mc Donagh, O. Mathieu, I. Osorio, C. Keesee, A. Morones, E. L. Petersen, W. Wang, T. A. DeVerter, et al., An experimental and modeling study of propene oxidation. part 2: Ignition delay time and flame speed measurements, *Combustion and Flame* 162 (2) (2015) 296–314.
- [54] A. Burcat, B. Ruscic, et al., Third millenium ideal gas and condensed phase thermochemical database for combustion (with update from active thermochemical tables)., Tech. rep., Argonne National Lab.(ANL), Argonne, IL (United States) (2005).
- [55] A. Stagni, A. Frassoldati, A. Cuoci, T. Faravelli, E. Ranzi, Skeletal mechanism reduction through species-targeted sensitivity analysis, *Combustion and Flame* 163 (2016) 382–393.
- [56] P. Pepiot-Desjardins, H. Pitsch, An efficient error-propagation-based reduction method for large chemical kinetic mechanisms, *Combustion and Flame* 154 (1-2) (2008) 67–81.
- [57] K. E. Niemeyer, C.-J. Sung, M. P. Raju, Skeletal mechanism generation for surrogate fuels using directed relation graph with error propagation and sensitivity analysis, *Combustion and flame* 157 (9) (2010) 1760–1770.
- [58] T. Poinso, D. Veynante, *Theoretical and numerical combustion*, RT Edwards, Inc., 2005.
- [59] R. Bilger, S. Stårner, R. Kee, On reduced mechanisms for methane air combustion in non-premixed flames, *Combustion and Flame* 80 (2) (1990) 135–149.
- [60] T. Farouk, F. Dryer, Microgravity droplet combustion: effect of tethering fiber on burning rate and flame structure, *Combustion Theory and Modelling* 15 (4) (2011) 487–515.
- [61] T. I. Farouk, F. L. Dryer, On the extinction characteristics of alcohol droplet combustion under microgravity conditions—a numerical study, *Combustion and flame* 159 (10) (2012) 3208–3223.

- [62] C. K. Law, Recent advances in droplet vaporization and combustion, *Progress in energy and combustion science* 8 (3) (1982) 171–201.
- [63] S. Prakash, W. Sirignano, Liquid fuel droplet heating with internal circulation, *International Journal of Heat and Mass Transfer* 21 (7) (1978) 885–895.
- [64] R. Kurose, H. Makino, S. Komori, M. Nakamura, F. Akamatsu, M. Katsuki, Effects of outflow from the surface of a sphere on drag, shear lift, and scalar diffusion, *Physics of Fluids* 15 (8) (2003) 2338–2351.
- [65] T. R. Jayawickrama, N. E. L. Haugen, M. U. Babler, M. A. Chishty, K. Umeki, The effect of stefan flow on the drag coefficient of spherical particles in a gas flow, *International Journal of Multiphase Flow* 117 (2019) 130–137.
- [66] S. S. Sadhal, P. S. Ayyaswamy, Flow past a liquid drop with a large non-uniform radial velocity, *Journal of Fluid Mechanics* 133 (1983) 65–81.
- [67] J. Li, Z. Zhao, A. Kazakov, M. Chaos, F. L. Dryer, J. J. Scire Jr, A comprehensive kinetic mechanism for CO, CH₂O, and CH₃OH combustion, *International Journal of Chemical Kinetics* 39 (3) (2007) 109–136.
- [68] M. Pelucchi, S. Namysl, E. Ranzi, A. Frassoldati, O. Herbinet, F. Battin-Leclerc, T. Faravelli, An experimental and kinetic modelling study of n-C₄H₆ aldehydes oxidation in a jet-stirred reactor, *Proceedings of the Combustion Institute* 37 (1) (2019) 389–397.
- [69] A. Lee, C. K. Law, An experimental investigation on the vaporization and combustion of methanol and ethanol droplets, *Combustion science and technology* 86 (1-6) (1992) 253–265.
- [70] B. Zhang, F. Williams, Alcohol droplet combustion, *Acta Astronautica* 39 (8) (1996) 599–603.
- [71] J. Leffler, H. T. Cullinan Jr, Variation of liquid diffusion coefficients with composition. dilute ternary systems, *Industrial & Engineering Chemistry Fundamentals* 9 (1) (1970) 88–93.
- [72] P. J. Roache, P. M. Knupp, Completed richardson extrapolation, *Communications in Numerical Methods in Engineering* 9 (5) (1993) 365–374.